PNAS RESEARCH ARTICLE | GENETICS

Microglia-derived extracellular vesicles trigger age-related neurodegeneration upon DNA damage

Ermioni S. Arvanitaki[a,b,1], Evi Goulielmaki[b,1], Katerina Gkirtzimanaki[b,1], George Niotis[a,b], Edisona Tsakani[a,b], Electra Nenedaki[a,b], Iliana Rouska[a,b], Mary Kefalogianni[c,d], Dionysios Xydias[d,e], Ilias Kalafatakis[b,f], Sotiris Psilodimitrakopoulos[d], Domna Karagogeos[b,f], Björn Schumacher[g,h], Emmanuel Stratakis[d], and George A. Garinis[a,b,2]

Edited by Hugo Bellen, Baylor College of Medicine, Houston, TX; received October 9, 2023; accepted March 22, 2024

DNA damage and neurodegenerative disorders are intimately linked but the underlying mechanism remains elusive. Here, we show that persistent DNA lesions in tissue-resident macrophages carrying an XPF-ERCC1 DNA repair defect trigger neuroinflammation and neuronal cell death in mice. We find that microglia accumulate dsDNAs and chromatin fragments in the cytosol, which are sensed thereby stimulating a viral-like immune response in *Er1*$^{Cx/-}$ and naturally aged murine brain. Cytosolic DNAs are packaged into extracellular vesicles (EVs) that are released from microglia and discharge their dsDNA cargo into IFN-responsive neurons triggering cell death. To remove cytosolic dsDNAs and prevent inflammation, we developed targeting EVs to deliver recombinant DNase I to *Er1*$^{Cx/-}$ brain microglia in vivo. We show that EV-mediated elimination of cytosolic dsDNAs is sufficient to prevent neuroinflammation, reduce neuronal apoptosis, and delay the onset of neurodegenerative symptoms in *Er1*$^{Cx/-}$ mice. Together, our findings unveil a causal mechanism leading to neuroinflammation and provide a rationalized therapeutic strategy against age-related neurodegeneration.

DNA damage | microglia | extracellular vesicles | neurodegeneration

Significance

Neuroinflammation is a major risk factor for challenging neurodegenerative disorders. Our study shows that persistent DNA damage leads to the accumulation of cytosolic DNA fragments in microglia, stimulating a viral-like immune response in *Er1*$^{Cx/-}$ and naturally aged mouse brains. We found that microglia release cytosolic DNAs in extracellular vesicles, causing neuronal cell death. Building on these findings, we developed an anti-inflammatory approach to target activated brain microglia in vivo, eliminate cytosolic DNAs, and postpone the early onset of neurodegeneration.

Accumulation of DNA damage is a hallmark of age-associated neurodegenerative diseases, such as Alzheimer's disease (1), (2), Parkinson's disease (3), Huntington's disease (4), and amyotrophic lateral sclerosis (5). In agreement, congenital DNA repair defects typically associate with neurological symptoms in man and corresponding animal models (6), (7). Irreparable DNA lesions inadvertently interfere with ongoing transcription in postmitotic neurons or obstruct the process of mRNA synthesis and DNA replication in dividing glial cells leading to cellular malfunction, senescence, or cell death (8), (9). To counteract DNA damage, mammalian cells rely on partially overlapping genome maintenance pathways to repair DNA lesions and preserve genome integrity (10).

Neuroinflammation is the activation of an innate immune response in the brain or spinal cord that often precedes neuronal tissue damage and degeneration (11), (12). Microglia, the resident phagocytes of the central nervous system (CNS), are phenotypically and developmentally distinct from peripheral or other tissue-resident macrophage populations and are ubiquitously distributed in the brain to support tissue maintenance and to safeguard the neuronal tissue against foreign pathogens and cellular debris (13). While transiently stimulated microglial cells offer protective effects for the brain, chronic activation leads to persistent release of inflammatory cytokines, overstimulating neuron receptors and causing subsequent damage to neuronal cells, thereby contributing to the premature onset of neurodegenerative disorders (14), (15). DNA damage–driven inflammation causally contributes to cellular malfunction and age-associated tissue degenerative changes (9), (16–20)–(20). However, the relative contribution of persistent DNA lesions in distinct cell types, e.g., neurons or glial cells to age-related neurodegeneration remains elusive.

XPF-ERCC1 (Xeroderma Pigmentosum F-Excision Repair Cross Complementation group 1), a heterodimeric endonuclease complex, is crucial for several DNA repair pathways repair, and for processing various noncanonical DNA structures that may interfere with replication, transcription, or DNA repair events (21–26). Mutations in XPF-ERCC1 in humans lead to Xeroderma Pigmentosum, XFE, or cerebro-oculo-facio-skeletal syndromes, characterized by premature aging features, including progressive neurodegeneration (27), (28). Likewise, animal models with inborn XPF-ERCC1 defects exhibit age-related pathologies, including cerebellar ataxia and cerebral atrophy (28). Using *Er1*$^{Cx/-}$ mice carrying an engineered XPF-ERCC1 defect only in tissue-resident macrophages, we provide evidence for a fundamental mechanism wherein irreparable DNA damage triggers sustained immune activation, leading to neuronal cell death. Importantly, our findings underscore a targeted intervention strategy against neuroinflammation and neurodegenerative disorders.

Author contributions: G.A.G. designed research; E.S.A., E.G., K.G., G.N., E.T., E.N., I.R., M.K., D.X., I.K., S.P., D.K., B.S., and E.S. performed research; E.S.A., E.G., K.G., G.N., E.T., E.N., I.R., M.K., D.X., I.K., S.P., D.K., and E.S. analyzed data; G.A.G. interpreted data; and G.A.G. wrote the paper.

The authors declare no competing interest.

This article is a PNAS Direct Submission.

[1]E.S.A., E.G., and K.G. contributed equally to this work.

[2]To whom correspondence may be addressed. Email: garinis@imbb.forth.gr.

This article contains supporting information online at https://www.pnas.org/lookup/suppl/doi:10.1073/pnas.2317402121/-/DCSupplemental.

Published April 18, 2024.

Results

Loss of ERCC1 in Tissue-Resident Macrophages Triggers Progressive Ataxia in Mice. Neuroinflammation, the innate immune response of the CNS (brain and spinal cord) to an inflammatory challenge, has recently emerged as a core feature of neurodegenerative diseases (13). Tissue-resident macrophages, e.g., brain microglia reside in distinct tissue environments and are vital for tissue homeostasis and defense against pathogens or environmental challenges (29).

To explore the role of brain-resident macrophages in responding to irreparable DNA lesions in vivo, we bred homozygous floxed *Ercc1* (*Ercc1*$^{F/F}$) animals with mice carrying the CX3C chemokine receptor (*Cx3cr)*1-Cre transgene in an *Ercc1* heterozygous background (hereafter referred to as *Er1*$^{Cx/-}$ animals). The *Cx3cr1* promoter was recently shown to be transiently active in neurons during mammalian development (30), (31) pointing to the use of *Cx3cr1*^{CreER} mice carrying a tamoxifen-inducible Cre allele as an alternative strategy for targeting microglia. However, tamoxifen is a potent genotoxin that indiscriminately triggers DNA damage to cells making it unsuitable for our studies (32), (33). Thus, we reevaluated the specificity of the constitutive original *Cx3cr1*-Cre transgene in our work. Confocal microscopy studies in brain cryosections and isolated microglia from *Cx3cr1-Cre* mice crossed with the Rosa YFP transgenic animals showed *Cx3cr1*-driven YFP expression in Macrophage-1 antigen (MAC1)$^+$ tissue-resident macrophages confirming the specificity of *Cx3cr1* promoter in microglial cells (34) (Fig. 1 *A* and *B* and *SI Appendix*, Fig. S1*A*). MAC1 (CD11b/CD18 heterodimer) is considered an acceptable marker for microglia and peripheral macrophages and TMEM119 can also be used as a selective microglia marker. The TMEM119-positive cell population does not differ from the MAC1-positive cell population in immunofluorescence studies of wt brain cryosections (*SI Appendix*, Fig. S1*B*). The specificity of *Cx3cr1-Cre* was also shown by absence of ERCC1 expression in isolated MAC1$^+$ microglial cells from *Er1*$^{Cx/-}$ animals expressing the *Cx3cr1*-Cre transgene compared to *Ercc1*$^{F/+}$ mice expressing the *Cx3cr1*-Cre transgene (hereafter referred to as wild-type; wt) (*SI Appendix*, Fig. S1*C*). Additionally, western blotting of whole cell extracts from Percoll fractions for the enrichment of microglia showed a reduction of ERCC1 expression levels in *Er1*$^{Cx/-}$ compared to wt cells (Fig. 1*C*). In agreement, we find that ERCC1 is expressed in different areas of the CNS, i.e., cerebellum, cerebral cortex, and spinal cord indicating the normative ERCC1 expression levels in *Er1*$^{Cx/-}$ cells other than the targeted cell population (Fig. 1*D* and *SI Appendix*, Fig. S1*D*). Last, western blotting of whole cell extracts from the brain and spinal cord confirmed the comparable ERCC1 expression levels in *Er1*$^{Cx/-}$ and wt animals (Fig. 1*E* and *SI Appendix*, Fig. S1*E*). Together, our findings support recent observations showing that the *Cx3cr1* promoter drives the expression of *Cre* recombinase largely restrictively in microglia even following excitatory injury (35). *Er1*$^{Cx/-}$ mice were born at the expected Mendelian frequency and presented no developmental defects or other pathological features. At 6 mo of age (24 wk), however, we observed progressive signs of ataxia in *Er1*$^{Cx/-}$ mice. When the 6-mo-old wt mice were suspended by their tails, the animals extended and swung their hind limbs to maintain balance (Movie S2). In contrast, *Er1*$^{Cx/-}$ mice kept their hind limbs in a clasped position (Fig. 1*F* and Movie S1) and walked with a wide gait compared to age-matched littermate control animals. Rotarod assessments demonstrated a notable hind limb coordination deficiency in the 6-mo-old *Er1*$^{Cx/-}$ animals compared to wt littermate controls (Fig. 1*G*). Beginning at 8 mo (32 wk) of age, *Er1*$^{Cx/-}$ animals develop kyphosis (Fig. 1*H*) and fine tremor to front legs. The early onset of neuropathological features in *Er1*$^{Cx/-}$ animals prompted us to assess the morphological and phenotypic characteristics of CNS-resident macrophages. Microglial cells in different CNS areas of 6-mo-old *Er1*$^{Cx/-}$ animals formed finger-like protrusions (Fig. 1*I* and *SI Appendix*, Fig. S1*F*). Next, we analyzed the morphology of microglia in the cerebellum using skeletal analysis on Iba1-stained sections. In *Er1*$^{Cx/-}$ microglia, we observed an increase in the number of junctions, triple junctions, and total length compared to wt microglia. Sholl analysis was applied to quantify the total number of intersections and the number of intersections relative to the radial distance from the individual cell soma. The total amount of *Er1*$^{Cx/-}$ process interceptions was higher than their wt counterparts. Interestingly, *Er1*$^{Cx/-}$microglia displayed a larger soma and an increase in primary and medial process intersections (*SI Appendix*, Fig. S2*A*). These changes in microglial morphology are indicative of microglial activation, a hallmark associated with altered cellular locomotion, increased antigen presentation, and enhanced proliferation status (36). Consistently, flow cytometry analysis revealed an increase in the expression of MHC-II (expressed only on antigen-presenting cells) and CD86 (constitutively expressed on activated macrophages) proteins in microglial cells from *Er1*$^{Cx/-}$ brains compared to wt controls (Fig. 1*J*). When compared to lipopolysaccharide-treated proinflammatory microglia, *Er1*$^{Cx/-}$ microglia cells exhibit a distinct MHC-II/CD86 expression profile (*SI Appendix*, Fig. S2*B*). In contrast to the antigen presentation profile, transmigration for LPS-treated wt microglia is lower compared to both untreated wt and *Er1*$^{Cx/-}$ microglial cells, supporting a different activation status between the *Er1*$^{Cx/-}$and bacterial toxin–treated cells (*SI Appendix*, Fig. S2*C*). These data are in agreement with previous findings showing that LPS treatment restricts microglia activation (37). Interestingly, transmigration using the Transwell™ chambers is higher for *Er1*$^{Cx/-}$ microglial cells compared to wt ones only in the presence of the chemoattractant, ATP (*SI Appendix*, Fig. S2*C*). The morphology of *Er1*$^{Cx/-}$ microglia, along with the MHC-II-CD86 expression and ATP-induced motility, argues for an inflammatory profile of these cells. A molecular switch that can modulate inflammatory responses is the signal transducer and activator of transcription 1 (STAT1), which is activated by the Janus Kinase (JAK) pathway in canonical interferon signaling and controls inflammation-related gene expression (38). Western blotting of whole cell extracts from microglia enriched Percoll fraction revealed an increase in both total STAT1 and phospho-STAT1 expression levels in *Er1*$^{Cx/-}$ compared to wt cells (Fig. 1*K*). Of note, prolonged incubation periods of rat primary microglia with LPS+IFN-γ were shown to induce both the expression levels of activated STAT1 (p-STAT1) and total-STAT1 (39). To explore the proliferation status of microglia, we report on the numbers of the CD11b$^+$CD45^{lo} population in wt and *Er1*$^{Cx/-}$ mice (36). CD45 is a type I transmembrane molecule that is expressed at higher levels on the surface of lymphocytes and peripheral monocytes and at lower levels on resident microglial cells. We find that the percentage of CD11b$^+$CD45^{lo} cells is comparable between the wt and *Er1*$^{Cx/-}$ 6-mo-old mice (Fig. 1*L* and *SI Appendix*, Fig. S3*A*). Further analysis in *Er1*$^{Cx/-}$ and wt brains showed that there is no significant difference in Annexin V $^+$ PI $^+$ cell populations gated for CD11b, indicating that *Er1*$^{Cx/-}$ brain microglia do not undergo apoptosis and that are tolerant to intrinsic DNA damage (*SI Appendix*, Fig. S3*B*). Next, we examined whether the observed microglia priming originates from peripheral immune cell infiltration in *Er1*$^{Cx/-}$ brains. H&E histological evaluation in the 6-mo-old *Er1*$^{Cx/-}$ brains revealed no inflammatory foci (*SI Appendix*, Fig. S3*C*). Moreover, the difference in the percentage of Ly6C$^+$ bone marrow-derived macrophages showed no statistical significance between *Er1*$^{Cx/-}$ and wt brains (Fig. 1*M*).

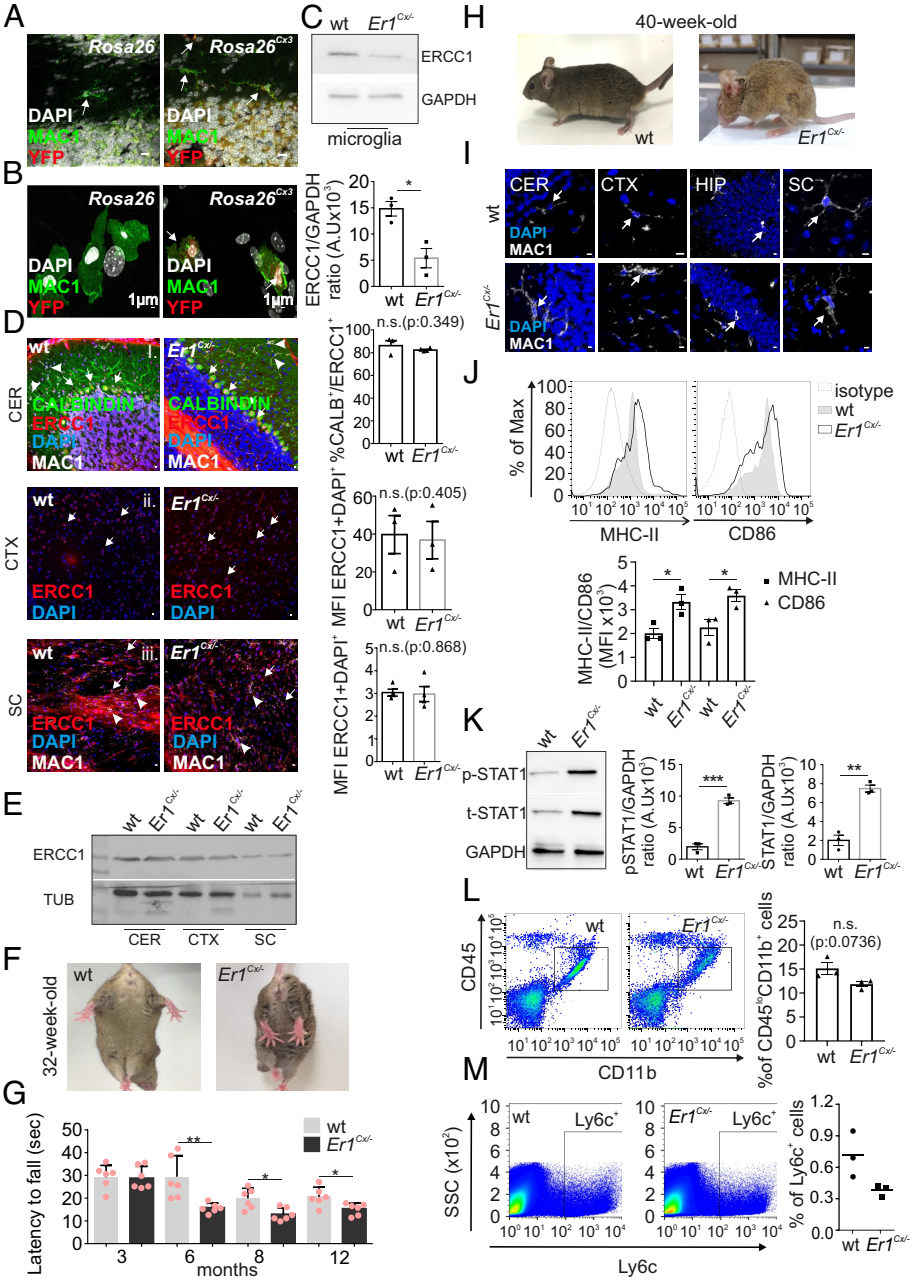

Fig. 1. Loss of ERCC1 in tissue-resident macrophages triggers progressive ataxia in mice. *Cx3cr1-Cre*-driven Rosa-YFP expression in (*A*), brain cryosections and (*B*) in isolated microglia. (*C*) Western blotting of ERCC1 protein in whole-cell extracts from the Percoll fraction of brains for the enrichment of microglia. GAPDH was used as a loading control. The graph represents ERCC1 protein levels normalized to GAPDH in $Er1^{Cx/-}$samples compared to corresponding wt controls. (*D*) Immunofluorescence staining of (*i*). ERCC1 and CALBINDIN (CALB) in mouse cerebella (indicated by the arrows). The numbers indicate the average percentage of ERCC1$^+$ CALB$^+$ ± SEM in $Er1^{Cx/-}$ and wt cerebella ($n > 70$ cells per genotype). (*ii* and *iii*) ERCC1 in cortex and spinal cord cryosections (indicated by the arrows). The numbers indicate the ERCC1 Mean Fluorescence Intensity (MFI) of DAPI$^+$ nuclei ($n > 5$ optical fields per genotype). Arrows indicate ERCC1$^+$ cells. Single-channel images are shown in *SI Appendix*, Fig. S1*D*. (*E*) Western blotting of ERCC1 protein in whole-cell extracts from different CNS areas. TUBULIN (TUB) was used as loading control. Graph is shown in *SI Appendix*, Fig. S1*E*. (*F*) A photograph of a 32-wk-old $Er1^{Cx/-}$ mouse and its control littermate depicting the hind limb paralysis developed in $Er1^{Cx/-}$ mice. (*G*) A graph depicting the latency to fall (seconds on the rotating rod) during rotarod assessment of the motor coordination of 3-, 6-, 8, and 12-mo-old $Er1^{Cx/-}$ mice and littermate wt controls, n = 6 mice per group (*H*). A photograph showing the kyphosis developed in 40-wk-old $Er1^{Cx/-}$ mice. (*I*) MAC1 immunofluorescent staining of microglia cells (indicated by arrows) in CER, CTX, HIP, and SC cryosections of $Er1^{Cx/-}$ and wt mice. Wider optical fields of the same pictures are shown in *SI Appendix*, Fig. S1*F*. (*J*) Activation status of Percoll-isolated microglia from $Er1^{Cx/-}$ mice and wt littermates. The histograms overlay MHC-II and CD86 expression of CD11b$^+$CD45^{lo} microglia cells (gating strategy shown in *SI Appendix*, Fig. S3*A*) from wt and $Er1^{Cx/-}$ brains. Isotype controls are indicated with a gray dotted line. The graph shows the respective MFIs. (*K*) Western blotting of total STAT1 and phospho-STAT1 protein in whole-cell extracts from microglia enriched Percoll fraction of brain tissue. GAPDH was used as loading control. The graph represents t-STAT1 and pSTAT1 protein levels normalized to GAPDH in $Er1^{Cx/-}$ samples compared to corresponding wt controls. (*L*) Flow cytometry analysis of Percoll-purified cells from 6-mo-old brains stained for CD11b and CD45. Representative flow cytometry plots show the gate for microglia, defined as the CD11b$^+$CD45^{lo} population. The graph depicts the percentage of microglia cells in wt and $Er1^{Cx/-}$ littermates. (gating strategy shown in *SI Appendix*, Fig. S3*A*). Statistical analysis indicated no significant differences. (*M*) Flow cytometry analysis of single-cell suspensions from $Er1^{Cx/-}$ and wt mouse brains. The graph depicts the percentage of Ly6C$^+$ cells. Statistical analysis indicated no significant differences. Cerebellum (CER), cortex (CTX), hippocampus (HIP), spinal cord (SC). Error bars indicate SEM among n ≥ 3 replicates, unless otherwise stated. The asterisk indicates the significance set at *P*-value: *≤0.05, **≤0.01 (two-tailed Student's *t* test). Scale bar: 10 μm, unless otherwise stated.

Consistently, the protein levels of CD45 were comparable between the 6-mo-old $Er1^{Cx/-}$ and wt brains (*SI Appendix*, Fig. S3*D*).

Accumulation of Cytoplasmic Chromatin Fragments Triggers a Type-I IFN Response in $Er1^{Cx/-}$ Microglia. Next, we sought to determine whether ablation of ERCC1 in microglia is sufficient to lead to constitutive DNA damage signaling. The phosphorylated Ataxia telangiectasia-mutated protein (pATM) is a central mediator of the DNA damage response. Moreover, phosphorylated histone H2A.X (γ-H2A.X)-containing foci accumulate at sites of DNA breaks (40). Confocal microscopy studies showed an increase in the number of $pATM^+/MAC1^+$ and $γ\text{-}H2A.X^+/MAC1^+$ cultured microglia deriving from $Er1^{Cx/-}$ brains compared to wt controls (*SI Appendix*, Fig. S4 *A* and *B*, as indicated). Consistently, the number of γ-H2A.X foci was higher in $Er1^{Cx/-}$ nuclei from cultured microglia or microglia cells in brain cryosections compared to respective wt controls (*SI Appendix*, Fig. S4*C*, Fig. S4*D*, respectively), indicating that irreparable DNA lesions accumulate in the genome of $Er1^{Cx/-}$ microglia cells.

DNA damage in the nucleus results in the accumulation of cytoplasmic DNA, notably in the form of micronuclei and cytoplasmic chromatin fragments (CCFs) or in DNA speckles (41). Our analysis showed that cytosolic dsDNAs accumulate in $Er1^{Cx/-}$ microglia from brain cryosections (*SI Appendix*, Fig. S4*E*) and in cultured $Er1^{Cx/-}$ microglial cells compared to the corresponding wt controls (*SI Appendix*, Fig. S4*F*; as indicated). Moreover, we find that DAPI stained foci (widely used in chromosome staining) colocalized with γ-H2A.X (also marking the presence of chromatin) in the cytoplasm of $Er1^{Cx/-}$ cultured microglial cells (*SI Appendix*, Fig. S4*G*). Further work revealed that pATM and γ-H2A.X foci accumulate in the cytoplasm of $Er1^{Cx/-}$ cells (*SI Appendix*, Fig. S4*H*; as indicated). Micronuclei and CCFs contain small chromosome fragments are often surrounded by nuclear envelope and associate with lamina disorganization and rupture (41). In our work, cytosolic chromatin fragments were positive for the DNA damage marker γ-H2A.X in $Er1^{Cx/-}$ cells but, unlike in micronuclei, they stained negative for lamin A/C or lamin B1 (*SI Appendix*, Fig. S4*I*). Consistently, staining with antibodies raised against lamin A/C or lamin B1 revealed no major perturbations in the nuclear lamina of microglial cells either in culture or in brain cryosections (*SI Appendix*, Fig. S4 *I* and *J*, as indicated). Absence of ERCC1 can lead to recombination events between telomeres and interstitial telomeric sequences and finally to shorter telomeres and circular products containing telomeric DNA (25). TelC in situ FISH, however, revealed no striking difference in the nuclear TelC fluorescence signal between $Er1^{Cx/-}$ and wt cultured microglial cells (*SI Appendix*, Fig. S5*A*). Finally, cytoplasmic DNA could also be a direct or indirect, due to replication fork collapse, result of R-loops and DNA lesions (42), (43). Replication fork stalling increases the exposure of ssDNA, allowing Replication Protein A (RPA)–coated ssDNA to trigger activation of ATR, which in turn drives activation of downstream targets, such as Chk1, MLL, and RPA itself (42), (44). To explore the possibility that $Er1^{Cx/-}$ cells are under replication stress, we performed IF analysis with phosphorylated-RPA (RPA32-S33). We found enrichment of nuclear RPA32-S33 in $Er1^{Cx/-}$ microglia compared to wt ones (*SI Appendix*, Fig. S5 *B* and *C* for cultured microglia, and brain cryosections respectively).

Genomic instability is often linked to the accumulation of cytoplasmic ssDNA (single-strand DNA) rather than of dsDNA as in $Er1^{Cx/-}$ microglia (43), (45). The latter led us to hypothesize that secondary structures of repetitive ssDNA sequences generate the dsDNA sequences. Strikingly, we find that $Er1^{Cx/-}$ cultured microglia accumulate lower levels of cytoplasmic ssDNA compared to wt microglia cells (*SI Appendix*, Fig. S5*D*). Moreover, cytoplasmic dsDNA fluorescence intensity in $Er1^{Cx/-}$ microglia cells was reduced upon recombinant Mung Bean S1 nuclease transfection (*SI Appendix*, Fig. S5*E*). Previous reports have shown that insufficient DNA damage repair in $Atm^{-/-}$ microglia results in active export of AT-rich repetitive elements in the cytoplasm (46). GSAT_MM, the major satellite repeat, was among the top-enriched AT-rich sequence in the cytosolic DNA of ATM-inhibited microglia. GSAT_MM levels were also higher in the cytosolic DNA of $Er1^{Cx/-}$ microglia compared to the DNA of wt ones (*SI Appendix*, Fig. S5*F*). The decrease of cytosolic dsDNA signal in $Er1^{Cx/-}$ cultured microglia upon S1 nuclease protein transfection and the accumulation of AT-rich sequences in the cytoplasm of $Er1^{Cx/-}$ cells suggest that reannealed ssDNA could be the origin of the $Er1^{Cx/-}$ related cytoplasmic dsDNA.

cGMP-AMP (cGAMP) synthase (cGAS) is a cytosolic sensor of microbial or self-dsDNA that was recently shown to sense cytoplasmic DNA due to nuclear DNA damage (41), (47). We find that cGAS accumulates in the cytoplasm of cultured $Er1^{Cx/-}$ microglia and in microglia from $Er1^{Cx/-}$ brain cryosections (*SI Appendix*, Fig. S6 *A* and *B* respectively). Moreover, cGAS colocalized with dsDNAs and with $DAPI^+/γ\text{-}H2AX^+$ foci in the cytosol of $Er1^{Cx/-}$ microglia (*SI Appendix*, Fig. S6*C*). To test whether nuclear DNA damage in $Er1^{Cx/-}$ microglia causally contributes to the accumulation of cytosolic dsDNAs in these cells, we next treated wt microglia with etoposide, a potent genotoxin that prevents religation of topoisomerase (TOP) II-mediated DNA double-strand breaks. Similar to $Er1^{Cx/-}$ microglia, we found that cytosolic dsDNAs accumulate in etoposide-treated wt cells (Fig. 2*A* and respective graph). Positive cells for colocalized cGAS and dsDNA or DAPI increased in $Er1^{Cx/-}$ cells and etoposide-treated wt cells (Fig. 2*A* and graph). However, in $Er1^{Cx/-}$ and wt^{ETO} cells cytoplasmic dsDNA/cGAS aggregates were more abundant compared to DAPI/cGAS fragments (Fig. 2*A* and graph). The specificity of dsDNA staining was further validated through DNase I treatment of wt and wt^{ETO} cultured microglia postfixation (*SI Appendix*, Fig. S6*E*).

The release of DNA into the cytosol stimulates STING (Stimulator of Interferon Genes) (48). Once phosphorylated by DNA sensors like cGAS, STING acts as a sensor of cyclic d-GMP and an adaptor protein mediating the IFN response. Type I IFNs execute antiviral functions (49) and under neuroinflammatory conditions, exert potent neurotoxic effects on the brain (50). Flow cytometry analysis revealed higher expression levels of pSTING in the brain and spinal cord microglia cells of 6-mo-old $Er1^{Cx/-}$ mice (Fig. 2*B* and *SI Appendix*, Fig. S6*F*). Consistently, the mRNA levels of *Ifnβ* and several interferon signature genes, including the interferon activated (*Ifi*) gene *207*, interferon regulatory factor *(Irf)1* and interferon-induced GTP-binding protein *Mx1* were higher in $Er1^{Cx/-}$ whole brain lysates compared to wt controls (Fig. 2*C*). Using the B16-Blue™ IFN-α/β cell line, we also found that the bioactive murine type-I IFN levels were higher in the extracellular milieu (brain lavage) of 6-mo-old $Er1^{Cx/-}$ brains compared to age-matched littermate controls (Fig. 2*D*). An ELISA showed comparable IFN-α levels between $Er1^{Cx/-}$ and wt brain lavages (*SI Appendix*, Fig. S6*G*). However, IFN-β western blotting revealed higher IFN-β protein levels in the $Er1^{Cx/-}$ cerebrospinal fluid (CSF) compared to wt controls (Fig. 2*E*). In line, the IFN-β levels were higher when we treated $Er1^{Cx/-}$ cells with brefeldin A, a protein transport inhibitor typically used to increase intracellular cytokine staining signal by blocking transport processes during cell activation (*SI Appendix*, Fig. S7*A*) (51). Likewise, IFN-β levels were higher in brefeldin A–treated wt microglia that were exposed to etoposide compared to untreated wt controls (*SI Appendix*,

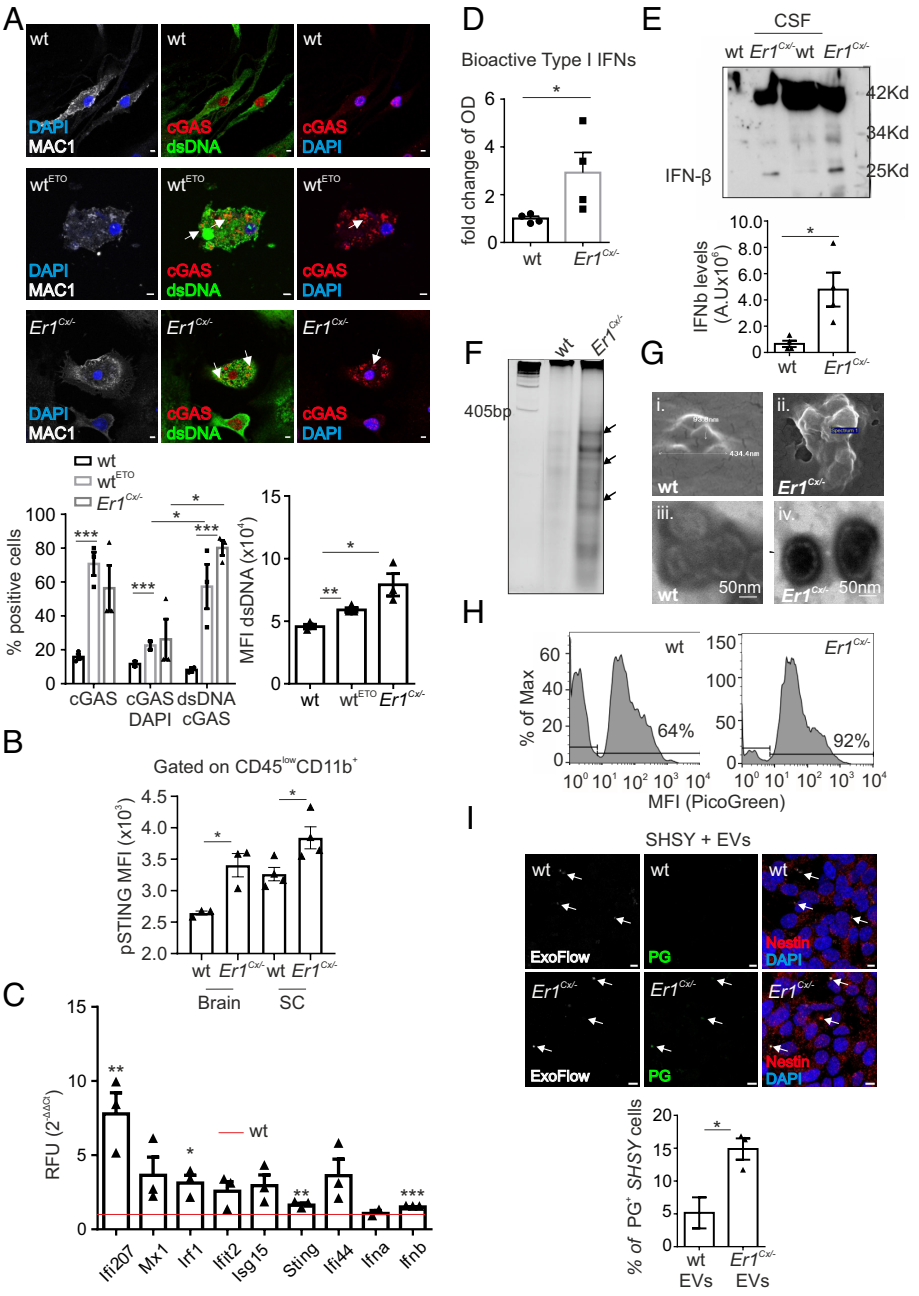

Fig. 2. DNA damage triggers the secretion of type I interferon and EVs carrying dsDNA. (*A*) Immunofluorescence detection of cGAS and dsDNA in cultured untreated wt, etoposide-treated wt, and untreated $Er1^{Cx/-}$ microglia. The graph depicts the percentage of cells with cytoplasmic cGAS$^+$, cGAS$^+$/DAPI$^+$ or dsDNA$^+$/cGAS$^+$ structures and the dsDNA MFI in cultured untreated and etoposide-treated wt and $Er1^{Cx/-}$ microglia. (*B*) The graph depicts the expression of pSTING (MFI) in pSTING$^+$ microglia in the brains or spinal cords (SC) of 6-mo-old $Er1^{Cx/-}$ and wt mice, purified with Percoll (n = 3 to 4). Microglia gating and representative histogram plots are shown in *SI Appendix*, Fig. S6*F*. (*C*) Quantitative PCR evaluation of the mRNA levels of interferon signature genes in the brain lysates of 6-mo-old wt and $Er1^{Cx/-}$ mice (as indicated; RFU: relative fluorescent units). (*D*) Type I IFN bioactivity (B16 reporter assay OD fold change) in 6-mo-old $Er1^{Cx/-}$ and age-matched wt brain lavages (n = 4). (*E*) Western blotting of IFN-β protein in CSF samples. Same volumes of CSF were used in each genotype. The graph represents IFN-β protein levels in wt and $Er1^{Cx/-}$ samples. (*F*) EVs isolated from 15 µL wt and $Er1^{Cx/-}$ CSF were subjected to phenol-chloroform DNA extraction, acrylamide gel electrophoresis, and EtBr staining. Experiment was repeated three times. (*G*) Scanning (*i* and *ii*) and Transmission (*iii* and *iv*) electron microscope images of circulating EVs purified from wt and $Er1^{Cx/-}$ brain lavages. The energy-dispersive-X ray spectra from $Er1^{Cx/-}$ EVs measured by the scanning electron microscope (*ii*) are shown in *SI Appendix*, Fig. S8*E*. (*H*) Flow cytometry analysis of purified EVs stained for CD11b and PicoGreen™. EVs were gated for CD11b (n = 3). A representative graph is presented in *SI Appendix*, Fig. S8*F*. (*I*) Immunofluorescence detection of PicoGreen in SH-SHY neurons incubated with wt and $Er1^{Cx/-}$ EVs, prestained with ExoFlow and PicoGreen. The cytoplasm of SH-SHY cells was labeled with Nestin. The arrows indicate ExoFlow-stained and/or PicoGreen-stained EVs. The graph depicts the percentage of PicoGreen$^+$ SH-SHY neuron cells. Error bars indicate SEM among n ≥ 3 replicates. Error bars indicate SEM among n ≥ 3 replicates. The asterisk indicates the significance set at *P*-value: *≤0.05, **≤0.01 (two-tailed Student's *t* test). (Scale bar: 5 µm.)

Fig. S7*A*). *Ercc1*$^{-/-}$ progeroid animals manifest several pathological features that closely resemble those seen in physiological aging (7), (27), (52). Staining of brain cryosections derived from young (2-mo-old) and old mice (24-mo-old) with MAC1 and γ-H2A.X showed that aged microglia present a higher number of nuclear γ-H2A.X foci compared to young microglia, indicating an age-linked genome instability (*SI Appendix*, Fig. S7*B*). In line with the cytosolic dsDNA phenotype of $Er1^{Cx/-}$ microglia, we also found that cytosolic dsDNA and cGAS accumulate in microglial cells of 24-mo-old, naturally aged mice compared to 2-mo-old young adult animals (*SI Appendix*, Fig. S7*C*). Consistently, the percentages of pSTING$^+$/CD11b$^+$ cells were higher in naturally aged brains (*SI Appendix*,

Fig. S7*D*). Thus, nuclear DNA damage triggers the accumulation of cytosolic dsDNAs and chromatin fragments in *Er1*$^{Cx/-}$ microglia, leading to the activation of the type-I IFN response in DNA repair-deficient mice and likely also with aging.

***Er1*$^{Cx/-}$ Microglia Secrete Extracellular Vesicles Loaded with Nucleic Acids.** We previously showed that persistent DNA damage accumulation in *Ercc1*$^{-/-}$ tissue-infiltrating macrophages triggers the release of extracellular vesicles (EVs), both in vivo and ex vivo (53). Microglia, when activated are also known to efficiently produce and release EVs efficiently (54). In our current study, *Er1*$^{Cx/-}$ microglia exhibited an increase in the expression of the EV marker CD9 and CD63 compared to wt control cells, indicating an EV-associated secretory phenotype (*SI Appendix*, Fig. S8 *A* and *B*). To isolate EVs from *Er1*$^{Cx/-}$ brain lavages, we performed sucrose gradient ultracentrifugation followed by flow cytometry analysis for the microglia maker CD11b. We found a higher abundance of microglia-derived (CD11b^{+}) EVs in the 6-mo-old *Er1*$^{Cx/-}$ brains compared to corresponding controls (*SI Appendix*, Fig. S8*C*). Importantly, western blot analysis showed a modest enrichment of CD11b, and a more prominent enrichment of the tetraspanin CD81, commonly used as a small EV marker (55) and of the DNA damage marker γ-H2A.X in EVs derived from *Er1*$^{Cx/-}$ brain lavages compared to corresponding wt controls (*SI Appendix*, Fig. S8*D*). Instead, the expression levels of the nonexosomal tethering protein EEA1, functioning in early endosome fusion, (56) were comparable between *Er1*$^{Cx/-}$ and wt control EVs. Together, these findings indicate that *Er1*$^{Cx/-}$ microglial cells secrete EVs loaded with cytosolic γH2AX^{+}-associated chromatin fragments. The DNA associated with the outer membrane of EVs is typically larger and mostly double-stranded, whereas both single-stranded (ss) and dsDNAs are abundant inside EVs (57). Phenol-chloroform DNA extraction from CSF-derived EVs followed by acrylamide gel electrophoresis and staining of nucleic acids with EtBr indicated the higher abundance of <400 bp DNA species in *Er1*$^{Cx/-}$ EVs compared to wt controls (Fig. 2*F*). Scanning and transmission electron microscopy of the vesicles derived from sucrose gradient fractionation of brain lavages revealed that microglia-derived EVs had a typical size of ~100 nm (Fig. 2 *G, i–iv*). Furthermore, *Er1*$^{Cx/-}$ vesicles appeared to carry a higher density cargo, evidenced by their darker center and the enriched phosphorus marking the presence of positively charged DNA moieties surrounded by a donut-shaped membrane (Fig. 2 *G, ii* and *iv* and *SI Appendix*, Fig. S8*E*). To further corroborate this finding, EVs isolated from the 6-mo-old *Er1*$^{Cx/-}$ and wt brain lavages were stained for CD11b and the fluorescent benzothiazole probe (PicoGreen) that specifically binds dsDNA. Flow cytometry analysis indicated that there is a higher percentage of microglia (CD11b^{+})-derived EVs loaded with dsDNAs in *Er1*$^{Cx/-}$ brain lavages compared to wt controls (Fig. 2*H* and *SI Appendix*, Fig. S8*F*).

Recent evidence suggests that EVs can transport proteins, RNA species, and DNA molecules between cells (58, 59)–(60). These findings prompted us to investigate whether *Er1*$^{Cx/-}$ microglia-derived EVs mediate the transport of cytosolic dsDNAs in neuronal cells. To test this, we incubated the SH-SHY neuronal cell line, marked with NESTIN-1, a known marker for neuronal progenitor cells (61), with ExoFlow- and PicoGreen-stained EVs derived from *Er1*$^{Cx/-}$ and wt brain lavages. Importantly, we detected a higher PicoGreen signal in neuronal cells incubated with *Er1*$^{Cx/-}$ EVs compared to wt control EVs for 16 h. Thus, *Er1*$^{Cx/-}$ microglia-derived EVs are able to target and efficiently discharge their dsDNA payload to recipient neurons (Fig. 2*I*).

***Er1*$^{Cx/-}$ Microglia Elicit an Antiviral-Like Response That Triggers Neuronal Cell Death.** Confocal microscopy of fluoromyelin and western blotting of Myelin Basic Protein (MBP)1 indicated that myelination is unaffected in 8-mo-old *Er1*$^{Cx/-}$ mice (*SI Appendix*, Fig. S9 *A* and *B*). Confocal microscopy studies in wt and *Er1*$^{Cx/-}$ brain cryosections showed no difference in the number of NeuN^{+} nuclei bearing γ-H2A.X foci between the two genotypes, further confirming the specificity of *Cx3cr1*-Cre (*SI Appendix*, Fig. S9*C*). However, we observed increased cell death in the Purkinje and granule cell layers of the cerebellum and in the dorsal root of the spinal cord in 6-mo-old *Er1*$^{Cx/-}$ mice (Fig. 3*A* and *SI Appendix*, Fig. S9*D*; as indicated). TUNEL fluorescence intensity was similar in the cortex of wt and *Er1*$^{Cx/-}$ animals of the same age (Fig. 3*A* and *SI Appendix*, Fig. S9*D*; as indicated). TUNEL positive and negative controls were performed on cryosections of wt cortices (*SI Appendix*, Fig. S9*E*). Consistently, flow cytometry analysis of 8-mo-old brain single-cell suspensions stained with Annexin V and Propidium Iodide revealed cell death in ~20 percent of *Er1*$^{Cx/-}$ cells (*SI Appendix*, Fig. S10*A*).

Once secreted, type I IFNs signal through type I-IFN receptor (IFNAR) in a paracrine and autocrine manner. The higher type I IFN protein levels and the increased expression of downstream effectors in *Er1*$^{Cx/-}$ brains (*SI Appendix*, Fig. S6*F* and Fig. 2 *C–E*) prompted us to test the IFNAR protein levels. Western blot analysis in whole cell extracts showed higher type I-IFN receptor (IFNAR) protein levels in *Er1*$^{Cx/-}$ cerebella and spinal cords compared to corresponding wt controls (Fig. 3*B*). Likewise, flow cytometry analysis indicated higher IFNAR protein levels in cells isolated from *Er1*$^{Cx/-}$ cerebella compared to wt controls (*SI Appendix*, Fig. S10*B*). Immunofluorescence studies further confirmed the pronounced expression of IFNAR in Purkinje and granule cells of the cerebellum and in cells localized at the dorsal and lateral spinal cord of *Er1*$^{Cx/-}$ mice (Fig. 3*C* and *SI Appendix*, Fig. S10*C*). The levels of IFNAR expression in wt and *Er1*$^{Cx/-}$ cortices were similar. Together, these data indicate that a fraction of neurons in the CNS of *Er1*$^{Cx/-}$ mice is sensitive to type I IFN stimuli. Consistently, immunofluorescence studies in different CNS areas of *Er1*$^{Cx/-}$ and wt mice that were intraperitoneally injected with brefeldin A indicated the accumulation of IFN-β in neuron cells located in the cortex, in Purkinje cells, in cells of the granular cerebellar layers (Fig. 3*D*) and in microglial (MAC1^{+}) cells across all CNS areas examined in *Er1*$^{Cx/-}$ mice (*SI Appendix*, Fig. S10*D*). These findings support recent observations demonstrating that, in addition to brain microglial cells, neurons can produce IFN-β as a result of extracellular IFN-β stimuli and/or intracellular signaling (62). In line with the IFN response in non-microglial cell populations, further analysis revealed the pronounced accumulation of cytosolic dsDNAs in Purkinje, granule cells, and cells of the molecular layer of the cerebellum, as well as in the dorsal and lateral spinal cord of *Er1*$^{Cx/-}$ mice compared to corresponding wt controls (Fig. 3*E* and *SI Appendix*, Fig. S11*A*). Postfixation DNase I treatment of *Er1*$^{Cx/-}$ cryosections reduced the dsDNA levels in MAC1^{+} cells as well as in PAX6^{+}/CALB^{+} cells, further arguing for the specificity of the dsDNA signal (*SI Appendix*, Fig. S11 *B* and *C*). Consistently, we found a higher percentage of CD11b^{-} pSTING^{+} cells in the 6-mo-old *Er1*$^{Cx/-}$ cerebella and spinal cords compared to age-matched wt controls (*SI Appendix*, Fig. S11*D*).

Microglia-Derived *Er1*$^{Cx/-}$ EVs Target IFN-α-Responsive Purkinje Cells Triggering Apoptosis. Our finding that *Er1*$^{Cx/-}$ microglia-derived EVs can target and discharge their dsDNA cargo in neuronal cells in vitro (Fig. 2 *F–I*) prompted us to hypothesize a similar scenario for *Er1*$^{Cx/-}$ animals. We reasoned that *Er1*$^{Cx/-}$ microglia package cytosolic dsDNAs into EVs, which are then released and target IFN-responsive, DNA repair-proficient neurons ultimately

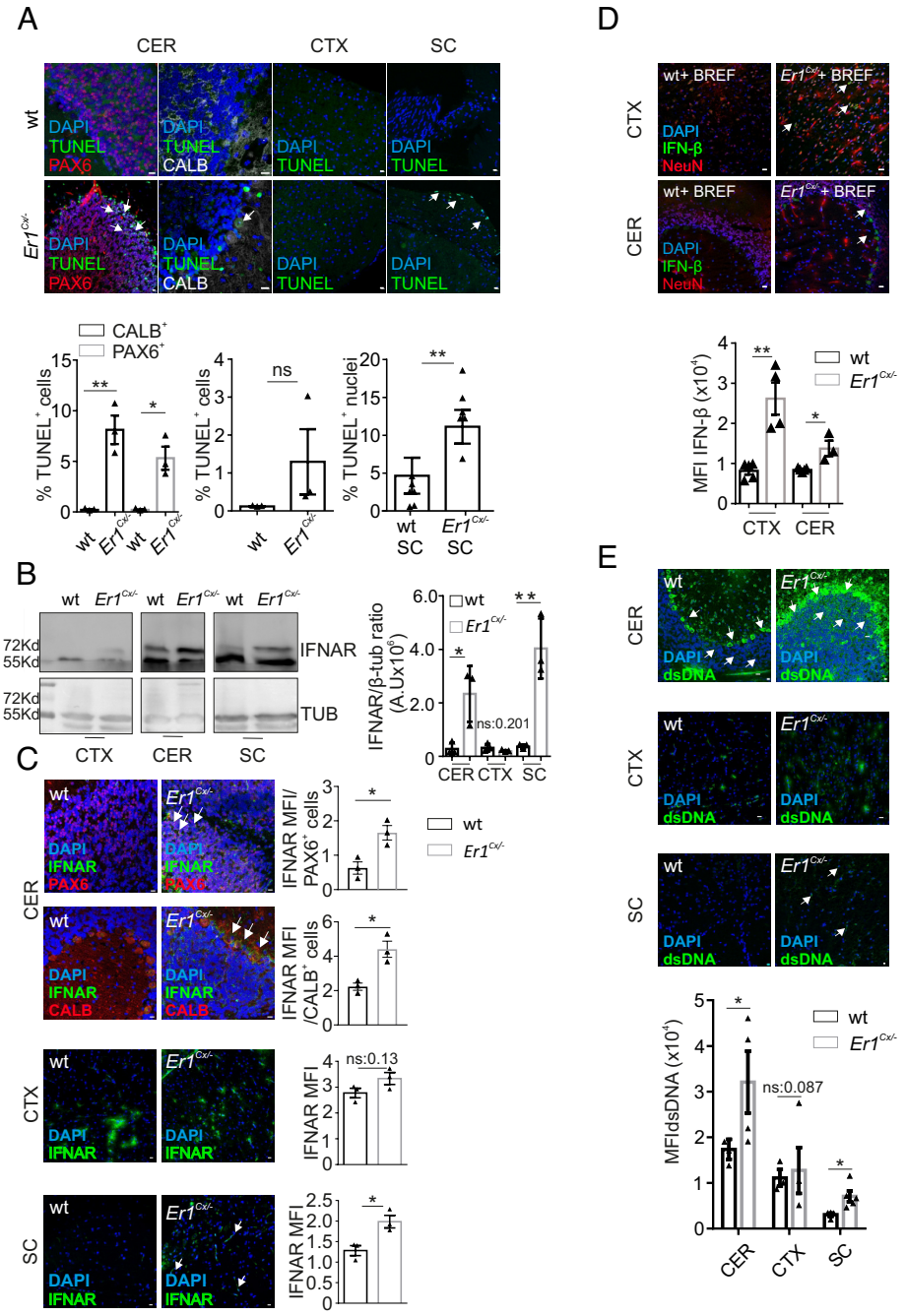

Fig. 3. Aged microglia elicit an antiviral-like response that leads to neuronal cell death. (*A*) Immunofluorescence detection of TUNEL$^+$ cells in the cerebellum (CER), cortex (CTX), and the periphery of spinal cord (SC). Arrows indicate only TUNEL$^+$ nuclei in the corresponding CNS regions of *Er1*$^{Cx/-}$ mice. The graphs depict the percentage of TUNEL$^+$CALB$^+$ or TUNEL$^+$PAX6$^+$ cells against the total number of CALB$^+$ or PAX6$^+$ cells (CER) and the percentage of TUNEL$^+$DAPI$^+$ cells against the total number of nuclei (CTX and SC) (n = 3 animals, n > 7 optical fields per mouse). Single channel images are shown in *SI Appendix*, Fig. S9*D*. (*B*) Western blotting of IFNAR protein in whole-cell extracts of CNS areas. TUBULIN (TUB) was used as a loading control. The graph represents the IFNAR densitometry analysis normalized to TUB. (*C*) Immunofluorescence detection of IFNAR in PAX6$^+$ and CALBINDIN$^+$ cells from cerebellar cryosections and in cryosections of cortices and spinal cords of *Er1*$^{Cx/-}$ and wt mice. Arrows indicate the cytoplasmic and membranous localization of IFNAR signal. The graphs depict the IFNAR MFI in indicated cell populations and areas (n > 7 optical fields per genotype). Single channel images are shown in *SI Appendix*, Fig. S10*C*. (*D*) Immunofluorescence detection of IFN-β in cryosections of different CNS regions from *Er1*$^{Cx/-}$ and wt mice injected intraperitoneally with Brefeldin A. Arrows indicate IFN-β-positive cells in the corresponding CNS regions. The graph depicts the IFN-β MFI in indicated areas. Immunofluorescence detection of IFN-β in MAC1$^+$ cells after Brefeldin A treatment is shown in *SI Appendix*, Fig. S10*D*. (*E*) Immunofluorescence detection of dsDNA in cryosections from different CNS regions of *Er1*$^{Cx/-}$ and wt mice. Arrows indicate dsDNA$^+$ cells in the corresponding regions. The graph depicts the dsDNA MFI in indicated areas. Single channel images are shown in *SI Appendix*, Fig. S11*A*. Error bars indicate SEM among n ≥ 3 replicates. The asterisk indicates the significance set at *P*-value: *≤0.05, **≤0.01 (two-tailed Student's *t* test). (Scale bar: 10 μm.)

leading to neuronal cell death and progressive neurodegeneration in *Er1*$^{Cx/-}$ animals. The latter would also explain the higher percentage of pSTING cells in the 6-mo-old *Er1*$^{Cx/-}$brains and spinal cords (*SI Appendix*, Fig. S11*D*), the higher IFNAR and IFN-β protein levels (Figs. 2*E* and 3 *B–D*) and the detection of cytosolic dsDNAs in distinct neuronal cell populations of the cerebellum (Purkinje cells) and the spinal cord (Fig. 3*E* and *SI Appendix*, Fig. S11 *A–C*). To test whether neurons are targeted by microglia-derived *Er1*$^{Cx/-}$ EVs, we focused our studies in Purkinje cells, a class of GABAergic inhibitory neurons that play pivotal roles in coordination, control, and locomotor learning. First, we treated cultures of acute wt brain slices with *Er1*$^{Cx/-}$ and wt EVs derived from 6-mo-old brains that

were previously labeled with the lipophilic green fluorescent dye PKH67. Next, we subjected wt brain slices to simultaneous 2 to 3 multiphoton microscope scanning (*SI Appendix*, Fig. S12 *A–C*) allowing us to monitor the selective uptake of microglia-derived $Er1^{Cx/-}$ EVs by CALBINDIN$^+$ cells in at least 200 μm detection depths. Our analysis showed that $Er1^{Cx/-}$ EVs efficiently target Purkinje cells compared to wt EVs; interestingly, the selective uptake of $Er1^{Cx/-}$ EVs by Purkinje cells was higher when brain slices were further treated with type I IFN (*SI Appendix*, Fig. S12*D*). When dsDNAs in EVs were prestained with PicoGreen, the colocalization of PicoGreen signal with CALBINDIN was more profound in those brain slices treated with $Er1^{Cx/-}$microglia-derived EVs compared to the ones treated with wt control EVs. Intriguingly, the higher uptake of $Er1^{Cx/-}$ EVs by Purkinje cells upon exposure to type I IFN was also followed by a higher PicoGreen uptake in these cells, indicating that the preferential targeting of $Er1^{Cx/-}$EVs is followed by the release of the $Er1^{Cx/-}$EV dsDNA cargo in recipient Purkinje cells (*SI Appendix*, Fig. S12*E*). Importantly, when we delivered ExoFlow-labeled EVs purified from $Er1^{Cx/-}$mice intranasally in wt mice and stained the wt cerebella with markers for neuronal cells (class III beta-tubulin—TuJ1), astrocytes (Glial fibrillary acidic protein—GFAP), and oligodendrocytes (adenomatous polyposis coli—CC1), we observed a high localization of ExoFlow puncta in neuronal cells of the cerebellum, primarily in the granule cell area. This does not exclude the possibility of $Er1^{Cx/-}$EV uptake in cell types adjacent to neurons. Additionally, a small percentage of ExoFlow puncta were observed in astrocytes and oligodendrocytes (*SI Appendix*, Fig. S13*A*). These findings align with our multiphoton microscopy results, further indicating that various neuronal cell types in the cerebellum beyond Purkinje cells can uptake $Er1^{Cx/-}$EVs. Finally, staining of acute brain slices with caspase-3 revealed that the exposure of type I IFN–treated brain slices to $Er1^{Cx/-}$ EVs for 6 h is sufficient to induce Purkinje cell death (*SI Appendix*, Fig. S13*B*). Thus, microglia-derived $Er1^{Cx/-}$ EVs preferentially target and release their dsDNA cargo to IFNAR$^+$ neurons, which are responsive to type I interferon, ultimately leading to apoptosis. To further explore the role of IFNAR in the type I interferon and EV-mediated neuronal cell death, we treated wt brain slices with $Er1^{Cx/-}$ EVs obtained from 6-mo-old brains. We utilized a blocking antibody against IFNAR or an isotype control antibody. Western blot analysis of protein extracts from the treated brain slices showed a reduction of cleaved caspase-3 protein levels after IFNAR blockade (*SI Appendix*, Fig. S13*C*). This aligns with our earlier findings, indicating a synergistic effect between type I interferon and $Er1^{Cx/-}$ EVs for the induction of neuronal cell death.

Intranasal Delivery of DNase I-Loaded EVs Reduces the DNA Damage–Driven Antiviral-Like Response and Neuronal Cell Death in $Er1^{Cx/-}$ Mice. To remove cytosolic dsDNAs from microglial cells and reduce the inflammatory load in $Er1^{Cx/-}$ brains, we next sought to develop an EV-based strategy to deliver recombinant DNase I nuclease and alleviate the dsDNA-mediated antiviral-like response in $Er1^{Cx/-}$ brains. To do so, we first used the NIH/3T3 cell line to generate EVs loaded with recombinant (pH-independent) DNase I. To selectively target DNase I EVs to microglia cells, the NIH3T3-derived EVs were coated with a custom anti-CD11b peptide derived from a combination of a CD63 binding sequence, i.e., CRHSQMTVTSRL (63) and the αMI-domain binding peptide CP05, i.e., RKLRSLWRR (64). Next, we used an intranasal delivery method as a noninvasive method to bypass the blood–brain barrier and deliver CD11b-ligand EVs to the brain and the spinal cord. Prior to the treatment, the CD11b-ligand EVs were labeled with the exosome-specific dye Exoflow. Immunofluorescence studies in mice treated intranasally with CD11b-ligand EVs revealed that targeting (CD11b ligand-coated) EVs show higher colocalization with microglial (MAC1$^+$) cells than the control (noncoated) EVs. Consistently, the ExoFlow dye was detected at similar levels in nonmicroglial (MAC1$^-$) cells across all animal groups tested (Fig. 4*A*). In an effort to identify the subset of microglial cells capable of uptaking EVs loaded with a protein cargo in vivo, we administered ExoFlow-stained, CD11b-ligand coated EVs containing a recombinant protein conjugated with YFP. Our observations indicate that approximately 30% of MAC1+ cells colocalized with labeled EVs, with the fluorescence from the exosome dye coinciding with the YFP fluorescence in all measured microglial cells (*SI Appendix*, Fig. S14*A*). Notably, the delivery of targeting DNase I EVs to etoposide-treated microglia ex vivo eliminated cytosolic dsDNAs and cGAS compared to empty (naïve) EVs (Fig. 4*B*). Having established that CD11b-ligand EVs loaded with DNase I can efficiently target microglia and remove cytosolic dsDNAs ex vivo, we next tested the in vivo efficacy of engineered targeting DNase I EVs in reducing neuroinflammation and neuronal cell death in the $Er1^{Cx/-}$ mice. To do so, targeting DNase I EVs were administered intranasally in 12-wk-old $Er1^{Cx/-}$ animals, twice a week and for 6 to 15 wk after treatment with a vasoconstrictor to prevent drainage of EVs from blood vessels into the tissues lining the nasal passages. We performed immunofluorescence studies in brain cryosections of $Er1^{Cx/-}$mice that had received targeting DNase I EVs intranasally, and observed a reduction in the levels of dsDNA in the cytoplasm of brain microglia in vivo (Fig. 4*C*). In agreement with this, an attenuation in the type I interferon response was also detected at 6 wk posttreatment, as measured by the type I IFN protein levels in $Er1^{Cx/-}$ brain lavages (Fig. 4*D*). Moreover, in vivo targeting of cytoplasmic DNA resulted in a lower percentage of MHC-II+CD86+ activated $Er1^{Cx/-}$ microglial cells 6 wk after the treatment, indicating a substantial reduction in neuroinflammation (Fig. 4*E* and *SI Appendix*, Fig. S14*B*). Importantly, the administration of targeting empty EVs kept the percentage of MHC-II+CD86+ wt microglial cells at low levels compared to the activated $Er1^{Cx/-}$ microglial cells (Fig. 4*E*). Besides $Er1^{Cx/-}$ microglia, treatment of $Er1^{Cx/-}$ mice with targeting DNase I EVs also reduced the PicoGreen-stained dsDNA signal of $Er1^{Cx/-}$ microglia-derived (CD11b$^+$) EVs (*SI Appendix*, Fig. S14*C*). Further work revealed that unlike with targeting naïve EVs, the intranasal administration of targeting DNase I EVs reduced the percentage of Annexin$^+$ PI$^-$ and Annexin$^+$ PI$^+$ cells in $Er1^{Cx/-}$ mice (Fig. 4*F* and *SI Appendix*, Fig. S14*D*). Strikingly, rotarod assessment of motor coordination in wt and $Er1^{Cx/-}$ mice treated with DNase I-loaded EVs showed an attenuation of the neurodegenerative symptoms in $Er1^{Cx/-}$ animals. Naïve and DNase I-loaded EVs treatment started at 12 wk of age and continued for 15 wk until the animals were 27 wk old. Animals receiving DNase I-loaded EVs exhibited the most prominent latency differences compared to animals receiving targeting naïve EVs between 21 and 27 wk of age (i.e., 9 and 15 wk of EV treatment respectively; Fig. 4*G*). Notably, wt mice receiving DNase I or naïve EVs showed no particular latency changes in the span of 15 wk of treatment (*SI Appendix*, Fig. S14*E*). Thus, the use of targeting DNase I EVs can efficiently remove cytosolic dsDNAs and reduce the antiviral-like response and neuronal cell death in $Er1^{Cx/-}$ mice, thereby providing a rationalized therapeutic strategy against age-related neuroinflammatory disorders.

Discussion

Until recently, endogenous DNA damage in postmitotic neurons was thought to be the primary cause of age-related neurodegenerative disorders seen in DNA repair-deficient patients and respective animal models (65). Besides neurons, brain degenerative changes involve the dysfunction of astrocytes, microglia, and oligodendrocytes, leading

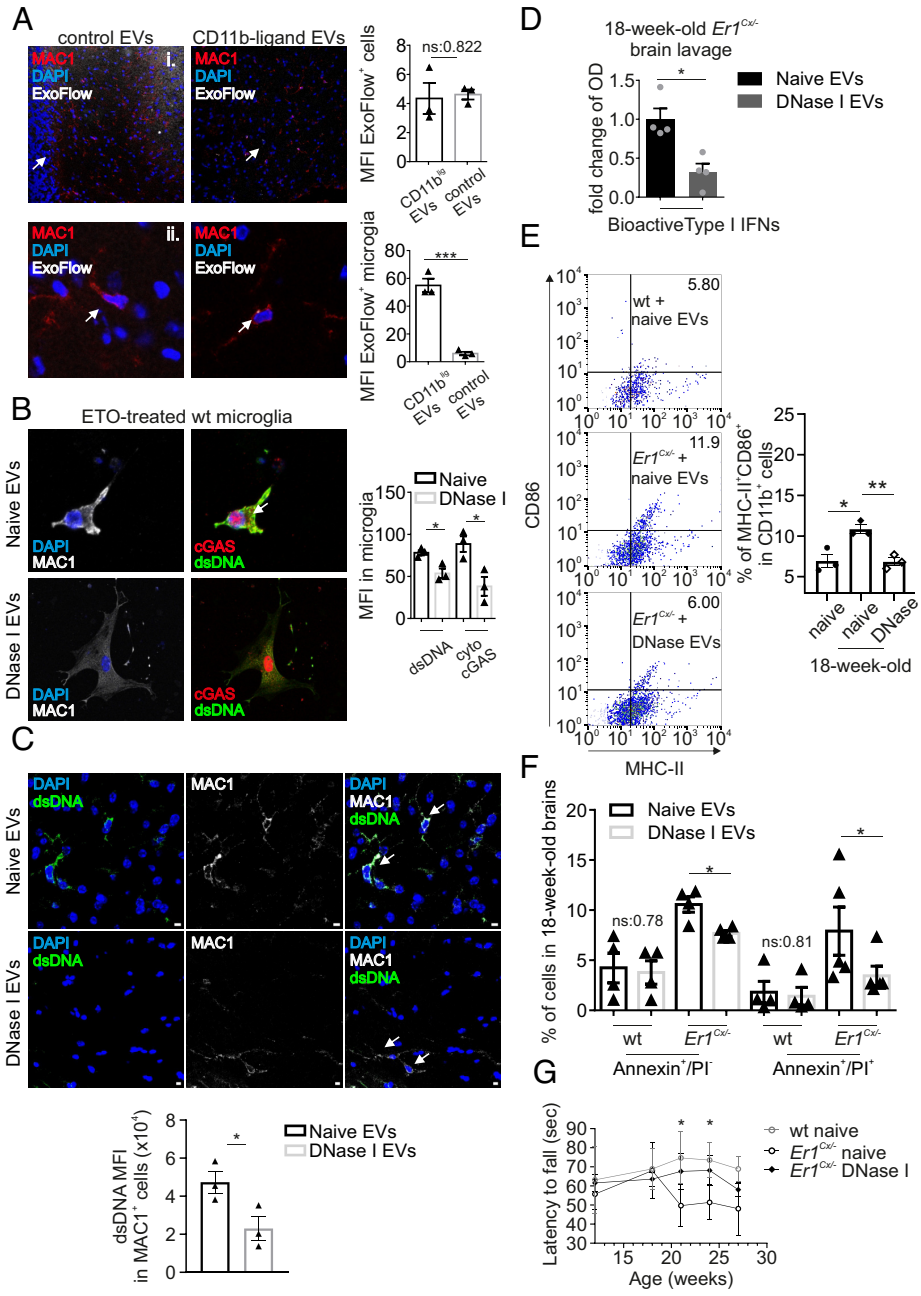

Fig. 4. CD11b-ligand decorated NIH-derived EVs loaded with DNase I preferentially target microglia cells ameliorating the antiviral-like response and neuronal cell death in *Er1*$^{Cx/-}$ mice. (*A*) Immunofluorescence detection of ExoFlow prestained EVs with or without CD11b-ligand decoration after intranasal administration in wt mice. Arrows indicate CD11b^{+}ExoFlow^{+} or CD11b^{-} ExoFlow^{+} cells. Graphs depict the percentage of CD11b^{+}ExoFlow^{+} or CD11b^{-}ExoFlow^{+} cells. (n > 1,000 cells counted in at least four optical fields each derived from three mice). (*B*) Immunofluorescence detection of MAC1, cGAS, and dsDNA in etoposide-treated wt microglia. Microglia was cultured in the presence of CD11b-ligand decorated EVs loaded with or without DNase (naïve EVs). The graph depicts cytoplasmic cGAS and dsDNA MFI in ETO-treated microglia cultured in the presence of naïve or DNase I-loaded EVs. (*C*) Immunofluorescence detection of dsDNA and MAC1 in brain cryosections of *Er1*$^{Cx/-}$ mice treated with DNase I-loaded or naïve EVs (30 Units of DNase I/administration, 12 to 30 intranasal instillations, once every 3 d). (n = 3) (*D*) Type I IFN bioactivity in the lavage of *Er1*$^{Cx/-}$mouse brains after intranasal administration of DNase I-loaded or naive EVs (12 intranasal instillations) (n = 4) (*E*) Flow cytometry analysis of brain single-cell suspensions stained for CD11b, MHC-II, and CD86. The graph depicts the percentage of MHC-II^{+}CD86^{+} microglial cells of 18-wk-old wt mice treated with naïve EVs and *Er1*$^{Cx/-}$ mice treated with DNase I-loaded or naive EVs (12 intranasal instillations). Gating strategy for microglia is shown in *SI Appendix*, Fig. S14*B*. (*F*) The graph depicts flow cytometry analysis of brain single-cell suspensions isolated from 18-wk-old *Er1*$^{Cx/-}$ or wt mice treated with DNase I-loaded or naive EVs stained for Annexin V and PI (as indicated, 12 intranasal instillations). Representative graphs are shown in *SI Appendix*, Fig. S14*D*. (*G*) Line graph depicting the motor coordination ability (latency to fall from the rod during rotarod assessment) of 3-mo-old wt mice receiving naïve EVs and *Er1*$^{Cx/-}$ mice receiving DNase I-loaded or naïve EVs for a time period of 15 wk (30 intranasal instillations). The respective graph showing wt mice treated with DNase I EVs is shown in *SI Appendix*, Fig. S14*E*. (n = 4). Error bars indicate SEM among n ≥ 3 replicates. The asterisk indicates the significance set at *P*-value: *≤0.05, **≤0.01 (two-tailed Student's *t* test).

to neuronal cell death (13, 14)–(15). Activated microglia exacerbate the inflammatory response observed in the course of Alzheimer's or Parkinson's disease and with aging (66–72). Moreover, microglia cells derived from Ataxia telangiectasia patients secrete neurotoxic factors that promote synaptic loss and neuronal apoptosis (73), (74). Consistently, the aberrant neuromotor impairment seen in mice deficient in nucleotide excision repair coincide with microgliosis, a reaction of CNS microglia to pathogenic stimuli (75), (76). Thus, microglial cells have a prominent role in neurodegeneration, irrespective of other cell-autonomous neuronal deficits.

Er1$^{Cx/-}$ mice are born at the expected Mendelian frequency, grow normally, are fertile, and show no visible pathological signs until adulthood. At 6 mo of age however, *Er1*$^{Cx/-}$ mice exhibit marked signs of ataxia, a common feature of several DNA damage–driven progerias (77) associated with neuronal cell death. This outcome is unexpected because in *Er1*$^{Cx/-}$ animals, neurons are proficient in DNA repair and do not accumulate DNA damage. Importantly, we find that γ-H2A.X-associated chromatin and dsDNAs build up in the cytosol of *Er1*$^{Cx/-}$ and naturally aged microglia, stimulating the cGAS–STING signaling pathway and a type I IFN response. Like *Er1*$^{Cx/-}$ microglia, wt microglia exposed to an exogenous genotoxin show the accumulation of cytosolic dsDNAs and cGAS aggregates. Similarly, *Atm*$^{-/-}$ microglial cells amass cytoplasmic DNAs, activating the cGAS–STING pathway and inducing a proinflammatory response in vitro. (74), (78). Cytosolic DNAs could originate from e.g., DNA damage–driven R-loops (79), (80), chromosome segregation defects (micronuclei) (43), rupture of the nuclear envelope (CCFs) (43) or defects in the regulation of DNA end resection during repair events and/or replication fork stalling due to DNA lesions (81) or non-B DNA structures (26), (46), (82).

DNA species translocate into the cytosol passively by mitotic-driven nuclear envelope breakdown (83) or actively by a CRM1-dependent mechanism (46), (79). The latter scenario may signify a physiological response of the nucleus to eliminate irreversibly damaged DNA fragments or byproducts of DNA damage repair. Our findings indicate that the cytosolic dsDNA identified in *Er1*$^{Cx/-}$ microglia may arise from the annealing of repetitive-sequence-rich ssDNA, a consequence of the accumulation of DNA lesions and replication fork stalling. Importantly, *Er1*$^{Cx/-}$ microglia secrete EVs carrying H2A.X-associated chromatin and cytosolic dsDNAs that target and deliver their dsDNA cargo to recipient neurons ex vivo triggering cell death. In agreement, we demonstrate that dsDNA fragments accumulate in distinct *Er1*$^{Cx/-}$ brain regions and the spinal cord, associated with increased IFNAR, p-STING, and IFN-β levels in these areas. Chronic exposure to increased type I IFN levels can trigger neuroinflammation and neurodegeneration (84). In our work, blocking the type I IFN receptor reduces the EV-mediated cell death in acute brain slices. Notably, the uptake of microglia-derived EVs by neurons is further pronounced when acute brain slices are treated with type I IFN. These findings indicate that the presence of microglial DNA in the cytosol of neuronal cells acts as an alarming, viral-like signal triggering widespread neuroinflammatory responses and ultimately leading to neurodegeneration.

EVs are nonimmunogenic carriers allowing their therapeutic cargo to circulate for extended periods within the body (85). To prevent neuroinflammation and potentially delay the premature onset of neurodegeneration in mice, we developed an EV-based strategy to deliver recombinant DNase I in primed *Er1*$^{Cx/-}$ microglia cells in vivo. Intranasal administration of targeting EVs decreased the accumulation of cytoplasmic microglial dsDNA but also of dsDNA content from microglia-derived *Er1*$^{Cx/-}$EVs further maximizing the beneficial outcome of our treatment. Removal of cytosolic DNAs by targeting EVs decreased the percentage of activated *Er1*$^{Cx/-}$microglia cells, reduced the IFN-β levels in brain lavages, lessened neuronal cell death, and rescued the motor deficit of *Er1*$^{Cx/-}$ animals. As DNase I-loaded EVs eliminate cytoplasmic dsDNA fragments from *Er1*$^{Cx/-}$ microglia, the EV DNase I treatment would also prevent microglia from entering the IFN response microglia state and being neurotoxic. Importantly, removal of cytosolic dsDNAs by targeted delivery of DNase I to microglia averts downstream immunogenic stimuli without interfering with antiviral responses or the homeostatic functions of the cGAS–STING pathway. Thus, as DNA damage–associated dsDNAs accumulate over time in the cytosol of microglia, an EV-based therapeutic scheme could offer a promising therapeutic strategy to combat age-related neuroinflammation and improve the outcome of neurodegenerative disorders associated with aging (16), (86).

Methods Details

Detailed materials and methods are provided in *SI Appendix*, including all materials and instruments, imaging procedures and all in vitro and in vivo biological assays. Key techniques and protocols used in this manuscript are summarized below.

Cell Culture. Microglial cells isolated from brains or spinal cords after collagenase dissociation and Percoll gradient purification were seeded on 24-well plates and cultured for 3 to 5 d in full DMEM.

Animal Studies. Animals homozygous for the floxed *Ercc1* allele (*Ercc1*$^{F/F}$) were intercrossed with mice carrying the *Cx3cr1-Cre* transgene to obtain inactivation of the *Ercc1* gene *Er1*$^{Cx/-}$ animals. Mice lacking the *Cx3cr1-Cre* transgene were used as wt controls (*Er1*$^{F/+}$, denotedas wt). All animal experiments received ethical approval by independent Animal Ethical Committee at IMBB-FORTH.

EV Isolation, Labeling, and Loading. EVs were purified from brain lavages or NIH/3T3 cells with the differential ultracentrifugation protocol and the sucrose gradient protocol when necessary. Purified EVs were then labeled and/or incubated with a CD11b-ligand and a non-NLS bearing signal peptide DNase I.

Data, Materials, and Software Availability. All study data are included in the article and/or supporting information.

ACKNOWLEDGMENTS. The Horizon 2020 Marie Curie ITN "HealthAge" (GA 812830), ELIDEK grants 631 and 1059 and 15546; the Fondation Santé; the "Research-Create-Innovate" actions (MIA-RTDI) "Panther" -00852 and "Liquid Pancreas" -00940 the Greece 2.0 National recovery and resilience plan Flagship program TAEDR–0535850 as well as the Uni-Pharma S.A. Greece and Pharmathen S.A research funds supported this work. The research work was supported by the third and fourth Call for HFRI PhD Fellowships (Nos. 11034 and 11330).

Author affiliations: [a]Department of Biology, University of Crete, Heraklion GR71409, Crete, Greece; [b]Institute of Molecular Biology and Biotechnology, Foundation for Research and Technology-Hellas, Heraklion GR70013, Crete, Greece; [c]Department of Physics, University of Crete, Heraklion GR71003, Crete, Greece; [d]Institute of Electronic Structure and Laser, Foundation for Research and Technology-Hellas, Heraklion GR71110, Crete, Greece; [e]Materials Science and Technology Department, University of Crete, Heraklion GR70013, Crete, Greece; [f]Medical School, Division of Basic Sciences, University of Crete, Heraklion GR71003, Crete, Greece; [g]Institute for Genome Stability in Ageing and Disease, Medical Faculty, University and University Hospital of Cologne, Cologne 50931, Germany; and [h]Cologne Excellence Cluster for Cellular Stress Responses in Ageing-Associated Diseases (CECAD), Center for Molecular Medicine Cologne (CMMC), University of Cologne, Cologne 50931, Germany

1. E. Adamec, J. P. Vonsattel, R. A. Nixon, DNA strand breaks in Alzheimer's disease. *Brain Res.* **849**, 67–77 (1999).
2. A. Nunomura *et al.*, Oxidative damage is the earliest event in Alzheimer disease. *J. Neuropathol. Exp. Neurol.* **60**, 759–767 (2001).
3. Z. I. Alam *et al.*, Oxidative DNA damage in the parkinsonian brain: An apparent selective increase in 8-hydroxyguanine levels in substantia nigra. *J. Neurochem.* **69**, 1196–1203 (1997).
4. T. Maiuri *et al.*, DNA damage repair in huntington's disease and other neurodegenerative diseases. *Neurotherapeutics* **16**, 948–956 (2019).
5. M. Bogdanov *et al.*, Increased oxidative damage to DNA in ALS patients. *Free Radic. Biol. Med.* **29**, 652–658 (2000).
6. P. J. McKinnon, DNA repair deficiency and neurological disease. *Nat. Rev. Neurosci.* **10**, 100–112 (2009).

7. M. Rieckher, G. A. Garinis, B. Schumacher, Molecular pathology of rare progeroid diseases. *Trends Mol. Med.* **27**, 907–922 (2021).
8. B. Schumacher, J. Pothof, J. Vijg, J. H. J. Hoeijmakers, The central role of DNA damage in the ageing process. *Nature* **592**, 695–703 (2021).
9. O. Chatzidoukaki, E. Goulielmaki, B. Schumacher, G. A. Garinis, DNA damage response and metabolic reprogramming in health and disease. *Trends Genet.* **36**, 777–791 (2020).
10. J. H. Hoeijmakers, Genome maintenance mechanisms for preventing cancer. *Nature* **411**, 366–374 (2001).
11. G. Welch, L. H. Tsai, Mechanisms of DNA damage-mediated neurotoxicity in neurodegenerative disease. *EMBO Rep.* **23**, e54217 (2022).
12. M. G. Tansey *et al.*, Inflammation and immune dysfunction in Parkinson disease. *Nat. Rev. Immunol.* **22**, 657–673 (2022).
13. C. K. Glass, K. Saijo, B. Winner, M. C. Marchetto, F. H. Gage, Mechanisms underlying inflammation in neurodegeneration. *Cell* **140**, 918–934 (2010).
14. M. L. Block, L. Zecca, J. S. Hong, Microglia-mediated neurotoxicity: Uncovering the molecular mechanisms. *Nat. Rev. Neurosci.* **8**, 57–69 (2007).
15. N. E. Gilhus, G. Deuschl, Neuroinflammation–a common thread in neurological disorders. *Nat. Rev. Neurol.* **15**, 429–430 (2019).
16. G. Chatzinikolaou, I. Karakasilioti, G. A. Garinis, DNA damage and innate immunity: Links and trade-offs. *Trends Immunol.* **35**, 429–435 (2014).
17. K. Stratigi, O. Chatzidoukaki, G. A. Garinis, DNA damage-induced inflammation and nuclear architecture. *Mech. Ageing Dev.* **165**, 17–26 (2017).
18. I. Karakasilioti *et al.*, DNA damage triggers a chronic autoinflammatory response, leading to fat depletion in NER progeria. *Cell Metab.* **18**, 403–415 (2013).
19. J. S. Tilstra *et al.*, NF-kappaB inhibition delays DNA damage-induced senescence and aging in mice. *J. Clin. Invest.* **122**, 2601–2612 (2012).
20. Y. Zhao, M. Simon, A. Seluanov, V. Gorbunova, DNA damage and repair in age-related inflammation. *Nat. Rev. Immunol.* **23**, 75–89 (2022).
21. Z. Apostolou, G. Chatzinikolaou, K. Stratigi, G. A. Garinis, Nucleotide excision repair and transcription-associated genome instability. *Bioessays* **41**, e1800201 (2019).
22. I. Kamileri, I. Karakasilioti, G. A. Garinis, Nucleotide excision repair: New tricks with old bricks. *Trends Genet.* **28**, 566–573 (2012).
23. L. J. Niedernhofer *et al.*, The structure-specific endonuclease Ercc1-Xpf is required to resolve DNA interstrand cross-link-induced double-strand breaks. *Mol. Cell Biol.* **24**, 5776–5787 (2004).
24. N. Kumar, S. Raja, B. Van Houten, The involvement of nucleotide excision repair proteins in the removal of oxidative DNA damage. *Nucleic Acids Res.* **48**, 11227–11243 (2020).
25. X. D. Zhu *et al.*, ERCC1/XPF removes the 3′ overhang from uncapped telomeres and represses formation of telomeric DNA-containing double minute chromosomes. *Mol. Cell* **12**, 1489–1498 (2003).
26. T. T. Li, K. M. Vasquez, Multi-faceted roles of ERCC1-XPF nuclease in processing non-B DNA structures. *DNA* **2**, 231–247 (2022).
27. L. J. Niedernhofer *et al.*, A new progeroid syndrome reveals that genotoxic stress suppresses the somatotroph axis. *Nature* **444**, 1038–1043 (2006).
28. S. Q. Gregg, A. R. Robinson, L. J. Niedernhofer, Physiological consequences of defects in ERCC1-XPF DNA repair endonuclease. *DNA Repair (Amst)* **10**, 781–791 (2011).
29. L. C. Davies, S. J. Jenkins, J. E. Allen, P. R. Taylor, Tissue-resident macrophages. *Nat. Immunol.* **14**, 986–995 (2013).
30. Z. Haimon *et al.*, Re-evaluating microglia expression profiles using RiboTag and cell isolation strategies. *Nat. Immunol.* **19**, 636–644 (2018).
31. B. Zhang *et al.*, The specificity and role of microglia in epileptogenesis in mouse models of tuberous sclerosis complex. *Epilepsia* **59**, 1796–1806 (2018).
32. D. H. Phillips, Understanding the genotoxicity of tamoxifen? *Carcinogenesis* **22**, 839–849 (2001).
33. V. Sahasrabuddhe, H. S. Ghosh, Cx3Cr1-Cre induction leads to microglial activation and IFN-1 signaling caused by DNA damage in early postnatal brain. *Cell Rep.* **38**, 110252 (2022).
34. S. Yona *et al.*, Fate mapping reveals origins and dynamics of monocytes and tissue macrophages under homeostasis. *Immunity* **38**, 79–91 (2013).
35. X. F. Zhao *et al.*, Targeting microglia using Cx3cr1-Cre lines: Revisiting the specificity. *eNeuro* **6**, ENEURO.0114-19.2019 (2019).
36. A. M. Jurga, M. Paleczna, K. Z. Kuter, Overview of general and discriminating markers of differential microglia phenotypes. *Front Cell Neurosci.* **14**, 198 (2020).
37. S. Lively, L. C. Schlichter, The microglial activation state regulates migration and roles of matrix-dissolving enzymes for invasion. *J. Neuroinflamm.* **10**, 75 (2013).
38. L. B. Ivashkiv, L. T. Donlin, Regulation of type I interferon responses. *Nat. Rev. Immunol.* **14**, 36–49 (2014).
39. Y. Zhao *et al.*, STAT1 contributes to microglial/macrophage inflammation and neurological dysfunction in a mouse model of traumatic brain injury. *J. Neurosci.* **42**, 7466–7481 (2022).
40. O. Fernandez-Capetillo, A. Lee, M. Nussenzweig, A. Nussenzweig, H2AX: The histone guardian of the genome. *DNA Repair* **3**, 959–967 (2004).
41. T. Li, Z. J. Chen, The cGAS-cGAMP-STING pathway connects DNA damage to inflammation, senescence, and cancer. *J. Exp. Med.* **215**, 1287–1299 (2018).
42. S. Saxena, L. Zou, Hallmarks of DNA replication stress. *Mol. Cell* **82**, 2298–2314 (2022).
43. K. N. Miller *et al.*, Cytoplasmic DNA: Sources, sensing, and role in aging and disease. *Cell* **184**, 5506–5526 (2021).
44. V. M. Vassin, R. W. Anantha, E. Sokolova, S. Kanner, J. A. Borowiec, Human RPA phosphorylation by ATR stimulates DNA synthesis and prevents ssDNA accumulation during DNA-replication stress. *J. Cell Sci.* **122**, 4070–4080 (2009).
45. F. Coquel, C. Neumayer, Y. L. Lin, P. Pasero, SAMHD1 and the innate immune response to cytosolic DNA during DNA replication. *Curr. Opin. Immunol.* **56**, 24–30 (2019).
46. X. Song *et al.*, DNA repair inhibition leads to active export of repetitive sequences to the cytoplasm triggering an inflammatory response. *J. Neurosci.* **41**, 9286–9307 (2021).
47. Z. Dou *et al.*, Cytoplasmic chromatin triggers inflammation in senescence and cancer. *Nature* **550**, 402–406 (2017).
48. J. Wu *et al.*, Cyclic GMP-AMP is an endogenous second messenger in innate immune signaling by cytosolic DNA. *Science* **339**, 826–830 (2013).
49. L. C. Platanias, Mechanisms of type-I- and type-II-interferon-mediated signalling. *Nat. Rev. Immunol.* **5**, 375–386 (2005).
50. S. Alboni *et al.*, N-acetyl-cysteine prevents toxic oxidative effects induced by IFN-alpha in human neurons. *Int. J. Neuropsychopharmacol.* **16**, 1849–1865 (2013).
51. S. B. Kovacs, C. Oh, Y. Aachoui, E. A. Miao, Evaluating cytokine production by flow cytometry using brefeldin A in mice. *STAR Protoc* **2**, 100244 (2021).
52. G. A. Garinis, G. T. van der Horst, J. Vijg, J. H. Hoeijmakers, DNA damage and ageing: New-age ideas for an age-old problem. *Nat. Cell Biol.* **10**, 1241–1247 (2008).
53. E. Goulielmaki *et al.*, Tissue-infiltrating macrophages mediate an exosome-based metabolic reprogramming upon DNA damage. *Nat. Commun.* **11**, 42 (2020).
54. M. Guo *et al.*, Microglial exosomes in neurodegenerative disease. *Front Mol. Neurosci.* **14**, 630808 (2021).
55. J. M. Escola *et al.*, Selective enrichment of tetraspan proteins on the internal vesicles of multivesicular endosomes and on exosomes secreted by human B-lymphocytes. *J. Biol. Chem.* **273**, 20121–20127 (1998).
56. R. Kamentseva *et al.*, Functional cycle of EEA1-positive early endosome: Direct evidence for pre-existing compartment of degradative pathway. *PLoS One* **15**, e0232532 (2020).
57. B. K. Thakur *et al.*, Double-stranded DNA in exosomes: A novel biomarker in cancer detection. *Cell Res.* **24**, 766–769 (2014).
58. J. Cai, G. Wu, P. A. Jose, C. Zeng, Functional transferred DNA within extracellular vesicles. *Exp. Cell Res.* **349**, 179–183 (2016).
59. A. Lanna *et al.*, An intercellular transfer of telomeres rescues T cells from senescence and promotes long-term immunological memory. *Nat. Cell Biol.* **24**, 1461–1474 (2022).
60. J. Cai *et al.*, Extracellular vesicle-mediated transfer of donor genomic DNA to recipient cells is a novel mechanism for genetic influence between cells. *J. Mol. Cell Biol.* **5**, 227–238 (2013).
61. A. Bernal, L. Arranz, Nestin-expressing progenitor cells: Function, identity and therapeutic implications. *Cell Mol. Life Sci.* **75**, 2177–2195 (2018).
62. E. V. Mesev, R. A. LeDesma, A. Ploss, Decoding type I and III interferon signalling during viral infection. *Nat. Microbiol.* **4**, 914–924 (2019).
63. X. Gao *et al.*, Anchor peptide captures, targets, and loads exosomes of diverse origins for diagnostics and therapy. *Sci. Transl. Med.* **10**, eaat0195 (2018).
64. N. P. Podolnikova, A. V. Podolnikov, T. A. Haas, V. K. Lishko, T. P. Ugarova, Ligand recognition specificity of leukocyte integrin alphaMbeta2 (Mac-1, CD11b/CD18) and its functional consequences. *Biochemistry* **54**, 1408–1420 (2015).
65. P. J. McKinnon, Genome integrity and disease prevention in the nervous system. *Genes Dev.* **31**, 1180–1194 (2017).
66. H. Quek *et al.*, ALS monocyte-derived microglia-like cells reveal cytoplasmic TDP-43 accumulation, DNA damage, and cell-specific impairment of phagocytosis associated with disease progression. *J. Neuroinflamm.* **19**, 58 (2022).
67. M. Y. Wendimu, S. B. Hooks, Microglia phenotypes in aging and neurodegenerative diseases. *Cells* **11**, 2091 (2022).
68. L. Muzio, A. Viotti, G. Martino, Microglia in neuroinflammation and neurodegeneration: From understanding to therapy. *Front Neurosci.* **15**, 742065 (2021).
69. S. Bachiller *et al.*, Microglia in neurological diseases: A road map to brain-disease dependent-inflammatory response. *Front Cell Neurosci.* **12**, 488 (2018).
70. L. Sevenich, Brain-resident microglia and blood-borne macrophages orchestrate central nervous system inflammation in neurodegenerative disorders and brain cancer. *Front Immunol.* **9**, 697 (2018).
71. H. J. Yoo, M. S. Kwon, Aged microglia in neurodegenerative diseases: Microglia lifespan and culture methods. *Front Aging Neurosci.* **13**, 766267 (2021).
72. S. Bido *et al.*, Microglia-specific overexpression of alpha-synuclein leads to severe dopaminergic neurodegeneration by phagocytic exhaustion and oxidative toxicity. *Nat. Commun.* **12**, 6237 (2021).
73. J. Bourseguin *et al.*, Persistent DNA damage associated with ATM kinase deficiency promotes microglial dysfunction. *Nucleic Acids Res.* **50**, 2700–2718 (2022).
74. X. Song, F. Ma, K. Herrup, Accumulation of cytoplasmic DNA due to ATM deficiency activates the microglial viral response system with neurotoxic consequences. *J. Neurosci.* **39**, 6378–6394 (2019).
75. M. C. de Waard *et al.*, Age-related motor neuron degeneration in DNA repair-deficient Ercc1 mice. *Acta Neuropathol.* **120**, 461–475 (2010).
76. G. S. Kajitani *et al.*, Neurovascular dysfunction and neuroinflammation in a Cockayne syndrome mouse model. *Aging (Albany NY)* **13**, 22710–22731 (2021).
77. F. Schnabel, U. Kornak, B. Wollnik, Premature aging disorders: A clinical and genetic compendium. *Clin. Genet.* **99**, 3–28 (2021).
78. H. Quek *et al.*, A rat model of ataxia-telangiectasia: Evidence for a neurodegenerative phenotype. *Hum. Mol. Genet.* **26**, 109–123 (2017).
79. O. Chatzidoukaki *et al.*, R-loops trigger the release of cytoplasmic ssDNAs leading to chronic inflammation upon DNA damage. *Sci. Adv.* **7**, eabj5769 (2021).
80. M. P. Crossley *et al.*, R-loop-derived cytoplasmic RNA-DNA hybrids activate an immune response. *Nature* **613**, 187–194 (2023).
81. J. Guan *et al.*, MLH1 deficiency-triggered DNA hyperexcision by exonuclease 1 activates the cGAS-STING pathway. *Cancer Cell* **39**, 109–121.e105 (2021).
82. R. Madabhushi *et al.*, Activity-induced DNA breaks govern the expression of neuronal early-response genes. *Cell* **161**, 1592–1605 (2015).
83. S. M. Harding *et al.*, Mitotic progression following DNA damage enables pattern recognition within micronuclei. *Nature* **548**, 466–470 (2017).
84. B. Viengkhou, M. J. Hofer, Breaking down the cellular responses to type I interferon neurotoxicity in the brain. *Front Immunol.* **14**, 1110593 (2023).
85. U. Sterzenbach *et al.*, Engineered exosomes as vehicles for biologically active proteins. *Mol. Ther.* **25**, 1269–1278 (2017).
86. A. Ioannidou, E. Goulielmaki, G. A. Garinis, DNA damage: From chronic inflammation to age-related deterioration. *Front Genet.* **7**, 187 (2016).